An Inside Look at Sunspot Oscillations with Higher Azimuthal Wavenumbers

David B. Jess[1,2], Tom Van Doorsselaere[3], Gary Verth[4], Viktor Fedun[5], S. Krishna Prasad[1], Robert Erdélyi[6], Peter H. Keys[1], Samuel D. T. Grant[1], Han Uitenbroek[7,8], and Damian J. Christian[2]

[1] Astrophysics Research Centre, Queen's University Belfast, Belfast Northern Ireland, BT7 1NN, UK; d.jess@qub.ac.uk
[2] Department of Physics and Astronomy, California State University Northridge, Northridge, CA 91330, USA
[3] Centre for mathematical Plasma Astrophysics Department of Mathematics, KU Leuven, Celestijnenlaan 200B bus 2400, B-3001 Heverlee, Belgium
[4] School of Mathematics and Statistics, The University of Sheffield, Hicks Building, Hounsfield Road, Sheffield, S3 7RH, UK
[5] Department of Automatic Control and Systems Engineering, University of Sheffield, Sheffield, S1 3JD, UK
[6] Solar Physics and Space Plasma Research Centre (SP²RC), The University of Sheffield, Hicks Building, Hounsfield Road Sheffield, S3 7RH, UK
[7] National Solar Observatory, University of Colorado Boulder, 3665 Discovery Drive, Boulder, CO 80303, USA
Received 2017 April 3; revised 2017 May 4; accepted 2017 May 15; published 2017 June 14

Abstract

Solar chromospheric observations of sunspot umbrae offer an exceptional view of magnetohydrodynamic wave phenomena. In recent years, a wealth of wave signatures related to propagating magneto-acoustic modes have been presented, which demonstrate complex spatial and temporal structuring of the wave components. Theoretical modeling has demonstrated how these ubiquitous waves are consistent with an $m = 0$ slow magneto-acoustic mode, which is excited by trapped sub-photospheric acoustic (p-mode) waves. However, the spectrum of umbral waves is broad, suggesting that the observed signatures represent the superposition of numerous frequencies and/or modes. We apply Fourier filtering, in both spatial and temporal domains, to extract chromospheric umbral wave characteristics consistent with an $m = 1$ slow magneto-acoustic mode. This identification has not been described before. Angular frequencies of 0.037 ± 0.007 rad s^{-1} (2.1 ± 0.4 deg s^{-1}, corresponding to a period ≈ 170 s) for the $m = 1$ mode are uncovered for spatial wavenumbers in the range of $0.45 < k < 0.90$ arcsec^{-1} (5000−9000 km). Theoretical dispersion relations are solved, with corresponding eigenfunctions computed, which allows the density perturbations to be investigated and compared with our observations. Such magnetohydrodynamic modeling confirms our interpretation that the identified wave signatures are the first direct observations of an $m = 1$ slow magneto-acoustic mode in the chromospheric umbra of a sunspot.

Key words: Sun: chromosphere – Sun: magnetic fields – Sun: oscillations – Sun: photosphere – sunspots

Supporting material: animation

1. Introduction

Since the early pioneering work by Beckers & Tallant (1969), Wittmann (1969), and Havnes (1970), to name but a few, oscillations and propagating waves tied to sunspot atmospheres have remained a challenging research area within solar physics. Observations have long indicated that wave power suppression exists in photospheric sunspot umbrae, with Nagashima et al. (2007) providing a high-resolution view of this phenomenon with the *Hinode*/SOT instrument. Many theories have been put forward to explain such power suppression, including the absorption, scattering, or channeling of field-guided magneto-acoustic waves following the mode conversion of p-mode oscillations (e.g., Braun et al. 1987; Cally 1995; Cally et al. 2003; Crouch & Cally 2003; Rijs et al. 2016), the less efficient excitation of wave activity due to reduced turbulent convection (e.g., Goldreich & Keeley 1977; Goldreich & Kumar 1988), and the reduction of attenuation lengths in the highly magnetic umbral regions of a sunspot (e.g., Jain et al. 1996; Hindman et al. 1997). What all of these theories have in common is the fact that the concentrated

umbral magnetic fields modify the emerging wave signatures to produce magneto-acoustic wave activity (Zharkov et al. 2013), which is observed to propagate anisotropically along the expanding magnetic field lines (see the recent reviews by Jess et al. 2015 and Verth & Jess 2016). The interplay between various plasma measurements (e.g., the magnetic field strength, the line-of-sight velocity, the intensity perturbations, etc., Fujimura & Tsuneta 2009; Freij et al. 2014; Moreels et al. 2015b) has allowed researchers to verify that the majority of visible wave signatures in sunspot umbrae are synonymous with the $m = 0$ slow magneto-acoustic mode. Indeed, such activity can readily be identified in chromospheric (e.g., Bloomfield et al. 2007; Vecchio et al. 2007; Kobanov et al. 2011; Jess et al. 2013; Löhner-Böttcher & Bello González 2015; Moreels et al. 2015a) and coronal (e.g., De Moortel 2006; McEwan & De Moortel 2006; Jess et al. 2012a, 2016; Krishna Prasad et al. 2012, 2015) sunspot-related studies involving both imaging and spectroscopic capabilities.

Observations of sunspot umbral atmospheres often show increased activity as one moves away from the photospheric layer. Socas-Navarro et al. (2009) revealed evidence for dynamic filamentary structures in the chromosphere of a sunspot umbra when observed in the Ca II H absorption line. Henriques & Kiselman (2013) and Henriques et al. (2015) found similar features, which were illuminated by the increased emission found in the vicinity of umbral flashes, suggesting that there may be convective processes still at work within the cooler, magnetically dominated umbral atmosphere, allowing wave motion to more readily disturb the lower density

---

chromospheric plasma (see, also, the recent review by Sych 2016). This has important consequences, since it means that in the more dynamic chromosphere, additional wave modes not readily identified (or suppressed) in the corresponding photosphere may present themselves more clearly. Gary (2001) devised a static model atmosphere of a solar active region and found that the plasma-β (ratio of the plasma pressure to the magnetic pressure) was consistently less than unity across all atmospheric heights, indicating that the magnetic field will continue to play an important role in the propagation of waves through the chromosphere (e.g., Yuan et al. 2014a; Löhner-Böttcher et al. 2016), often creating radial structuring of the oscillation signals depending on the strength and orientation of the localized magnetic field, which are clearly visible in the Fourier power spectra maps presented by Reznikova et al. (2012) and Sych & Nakariakov (2014).

Modeling efforts focused on the excitation, propagation, and/or dissipation of compressive waves in simplified solar atmospheres have been developed over a number of decades, with earlier examples including the work of Cram & Wilson (1975), Schmieder (1977), and Ulmschneider et al. (1977), to name but a few. More recent models have been constructed by, e.g., Khomenko & Collados (2006), Khomenko et al. (2008), Fedun et al. (2011a), Vigeesh et al. (2012), Cally & Moradi (2013), Santamaria et al. (2015), Santamaria et al. (2016), and Cally (2017). The excitation of longitudinal waves have been shown to be a consequence of the convective massaging of flux tubes (magnetic pumping, Kato et al. 2011, 2016), while, on the other hand, Krishna Prasad et al. (2015) have observationally shown that their generation is rather connected to p-mode oscillations. The propagation of Alfvén waves in magnetic pores, and its potential for seismology, was described by Fedun et al. (2011b), Mumford & Erdélyi (2015), and Mumford et al. (2015), with their observational signatures computed by Shelyag & Przybylski (2014). The effect of neutrals on their dissipation and the resulting heating was further studied by Arber et al. (2016) and Shelyag et al. (2016).

Importantly, in recent years, we have developed better imaging detectors that are more sensitive to incident photons. The benefits of this are twofold: (1) higher sensitivity equates to shorter exposure times, which helps to "freeze" atmospheric seeing when acquiring observations from ground-based facilities to help prevent spatial degradation, and (2) shorter exposure times allow for higher cadence image sequences, which raises the intrinsic Nyquist limit and allows us to probe high-frequency oscillations and propagating waves (see Chapter 2 in the review by Jess et al. 2015). Furthermore, better and more-robust adaptive optics systems are allowing longer duration studies of solar phenomena to be captured, providing a much improved frequency resolution for pinpointing and segregating particular oscillations of interest. Therefore, we are in an era where we can finally probe and examine the signatures and characteristics resulting from the superposition of multiple wave modes and harmonics within a single data set. Here, in this article, we employ modern processing techniques to extract, interpret, and model, for the first time, higher-order wave modes found within a sunspot umbral atmosphere.

2. Observations and Processing

The data set used here has been thoroughly documented in previous studies (e.g., Jess et al. 2013, 2016; Krishna Prasad

et al. 2015). However, for completeness, we will provide a brief overview. The image sequence duration was 75 minutes and was obtained during excellent seeing conditions between 16:10–17:25 UT on 2011 December 10 with the Dunn Solar Telescope (DST) at Sacramento Peak, New Mexico. The Rapid Oscillations in the Solar Atmosphere (ROSA; Jess et al. 2010) and Hydrogen-Alpha Rapid Dynamics camera (HARDcam; Jess et al. 2012a) imaging systems were utilized to capture the near circularly symmetric sunspot present within active region NOAA 11366, which was positioned at heliocentric coordinates (356″, 305″), or N17.9W22.5 in the conventional heliographic coordinate system. Here, we employ the blue continuum (52 Å bandpass filter centered at 4170 Å) and Hα (0.25 Å filter centered on the line core at 6562.8 Å) filtergrams, with platescales of 0″069 and 0″138 per pixel, respectively, to provide a field-of-view size equal to 71″ × 71″. High-order adaptive optics (Rimmele 2004) and speckle reconstruction algorithms (Wöger et al. 2008) were implemented to improve the final data products, with final cadences of the continuum and Hα channels equal to 2.11 s and 1.78 s, respectively. The Helioseismic and Magnetic Imager (HMI; Schou et al. 2012) present on the *Solar Dynamics Observatory* (*SDO*; Pesnell et al. 2012) provided simultaneous vector magnetograms of the active region with a cadence of 720 s and a two-pixel spatial resolution of 1″0. A contextual HMI continuum image was also employed to co-align the images obtained from the DST with the full-disk HMI observations. Once aligned, a time-averaged 4170 Å continuum image was used to determine the umbral center-of-gravity, or intensity "barycenter," which forms the central coordinates of the umbral annulus used in Section 3. Sample images of the data employed here are displayed in Figure 1.

3. Analysis and Discussion

An image sequence obtained at the core of the Hα line profile is employed to examine wave-related activity in the solar chromosphere for three distinct reasons. First, even with the reduced opacities present in the sunspot umbra, there is no evidence in our Hα observations of umbral flash behavior, which dominates data sets obtained at the core of the Ca II H/K or Ca II 8542 Å absorption profiles. Grant et al. (2017) have shown statistically that umbral flashes first appear at an optical depth of log $\tau \sim -3$, and preferentially manifest at an optical depth of log $\tau \sim -4.6$, corresponding to approximate geometrical heights of ~250 km and ~750 km, respectively (sunspot model "M"; Maltby et al. 1986). Therefore, with this in mind, our Hα umbral observations are likely to be formed at heights above 750 km, thus avoiding contamination from umbral flash events and making the visible intensity fluctuations purely related to the embedded (non-shocked) wave activity. Second, as the modeling efforts of Leenaarts et al. (2012, 2013) have revealed, the opacity of the Hα line in the upper chromosphere is only weakly sensitive to the localized temperature, thus further reducing its sensitivity to high-forming umbral flash behavior. Third, the time cadence of the Hα observations is the highest (1.78 s), thus providing the best possible temporal frequency coverage, while still maintaining a diffraction-limited spatial resolution.

The work of Jess et al. (2013) employed temporal filtering of the Hα time series to provide a thorough understanding of dominant periodicities as a function of radial distance from the center of the umbra (or umbral "barycenter"). For the purposes
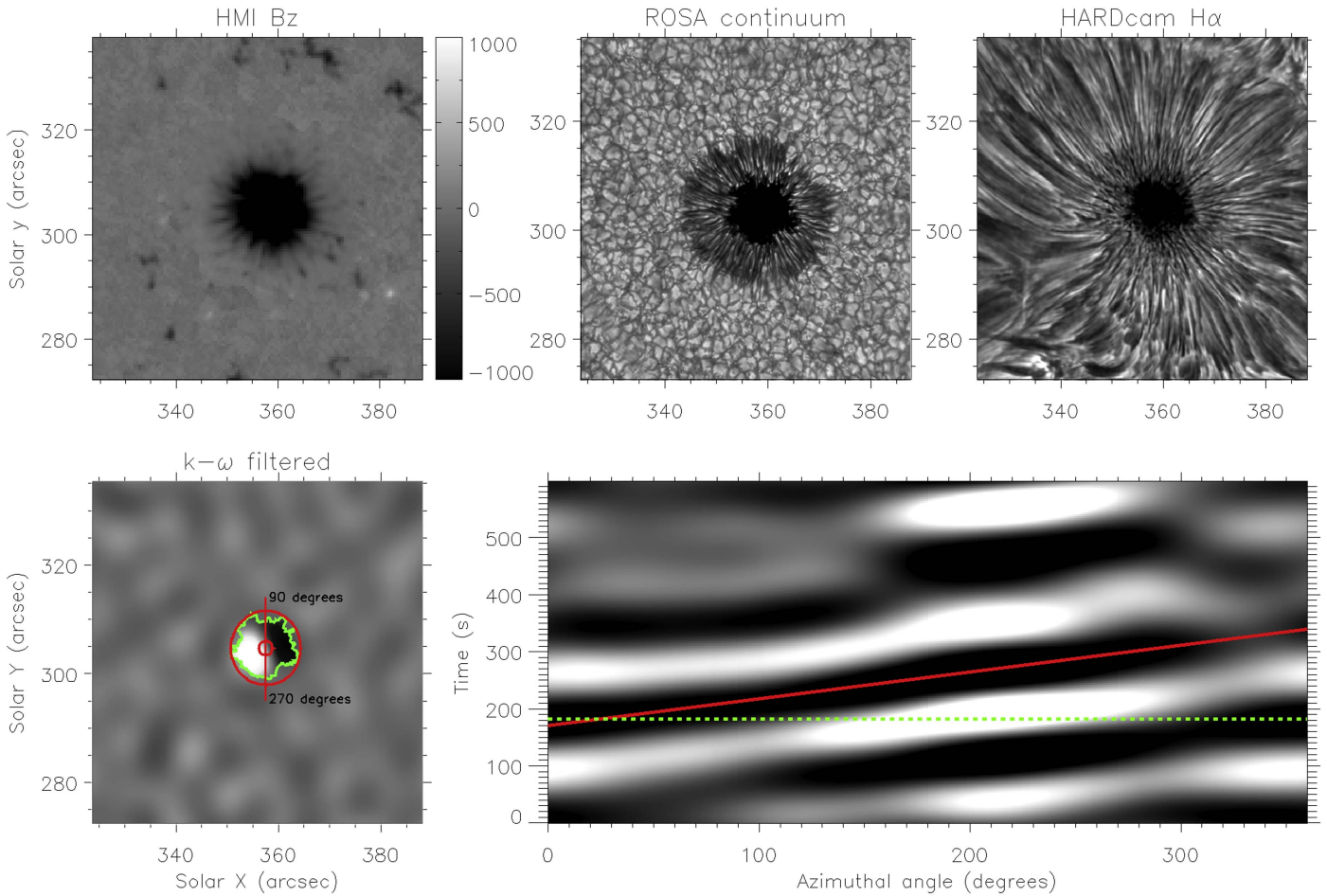
Figure 1. Sample images of active region NOAA 11366 revealing the vertical component of the magnetic field (B_z; upper left), the 4170 Å continuum (upper middle), and the narrowband Hα line core (upper right). The color bar corresponding to the strength of the magnetic field is saturated at ± 1000 G to better identify the sunspot structure. The lower left panel displays a snapshot of Hα intensities following both temporal and spatial frequency filtering. The green contour outlines the time-averaged umbra/penumbra boundary, while the red annulus depicts the extent of the region used for examining azimuthal wave motion within the umbra, where the center of the annulus is placed at the umbral barycenter. The lower right panel is a time–azimuth diagram following the polar transformation of the signals contained within the red annulus in the lower left panel, which allows the circular nature of the wave rotation to be investigated in a similar way to traditional time–distance diagrams. The horizontal dashed green line highlights the azimuthal intensity signal corresponding to the filtered image shown in the lower left panel, which is also plotted in Figure 3, while the solid red line represents the fitted angular frequency of the rotating wave amplitudes.

of that work, no filtering was performed in the spatial domain. However, examining time-lapse movies of the temporally filtered Hα images reveals a plethora of dynamic wave activity across a variety of spatial scales, particularly within the umbra where a dominant periodicity of ~180 s was uncovered, which is consistent with the work of Kobanov et al. (2011, 2013, 2015). The enhanced oscillations, which are clearly observed in the temporally (150–180 s) filtered Hα observations, are similar in magnitude to the outputs of chromospheric umbral resonance models put forward by Zhugzhda & Locans (1981) and Staude et al. (1985), whereby the upwardly propagating slow magneto-acoustic waves, which do not violate the acoustic cut-off period (e.g., Bel & Leroy 1977; Fleck & Schmitz 1991; Zhugzhda 2008; Yuan et al. 2014b; Snow et al. 2015, to name but a few), are reflected continuously between the steep temperature gradients present close to the photospheric temperature minimum and at the transition region boundary. Of course, temperature and density gradients within the umbra provide a non-ideal resonator, which in turn gives wave amplitude inhomogeneities across the magnetic waveguide, similar to what is seen in the upper right panel of Figure 3. These effects have been investigated previously by Locans et al. (1988), and

more recently by Norton (2000), Norton & Ulrich (2000), Christopoulou et al. (2003), Botha et al. (2011), and the review by Khomenko & Collados (2015), with observational evidence for such a scenario found by Moreels et al. (2015a). However, importantly, the temporally filtered time series indicates that a component of the observed umbral oscillations are occurring on much larger spatial scales than previously uncovered.

To isolate and examine the presence of large-scale umbral oscillations, a complete k–ω filtering process was applied to the Hα data, where k is the spatial wavenumber (equal to $\frac{2\pi}{\lambda}$, where λ is the spatial wavelength) and ω is the temporal frequency. Following the work of Jess et al. (2013), a relatively broad temporal bandpass filter corresponding to 160–200 s (or $5.0 < \omega < 6.3$ mHz) was employed to extract the dominant umbral oscillations. To examine the larger spatial fluctuations, a filter covering $7''–14''$ (or $0.45 < k < 0.90$ arcsec^{-1}) was chosen, as highlighted by the solid black box in Figure 2. This wavenumber range was chosen since the diameter of the sunspot umbra is ≈98 pixels (see the outer edge of the annulus shown in Figure 3), corresponding to ≈13″.5, which means a spatial filter spanning $7''–14''$ will allow coherent oscillations of

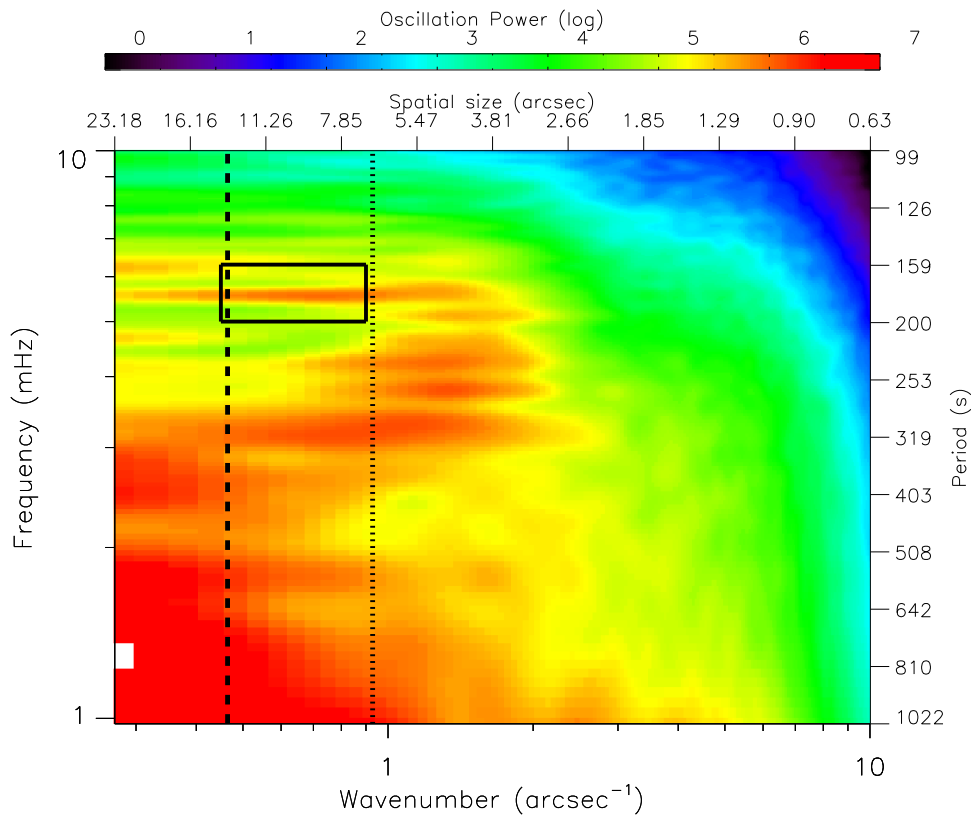**Figure 2.** k–ω diagram, cropped to display spatial wavenumbers in the range of $0.27 < k < 10.02$ arcsec^{-1} ($23''18$–$0''63$) and temporal frequencies in the range of $0.98 < \omega < 10.00$ mHz (99–1022 s). The colors represent oscillatory power, shown on a log-scale, where red represents seven orders of magnitude higher power than the background. The vertical dashed line corresponds to the spatial size of the umbral diameter ($\approx 13''5$), while the vertical dotted line represents the spatial size corresponding to the radius of the umbra ($\approx 6''75$). The solid black box highlights the FWHM of the chosen k–ω filter, which is seen to encapsulate a band of excess power at ≈ 170 s over the entire spatial extent of the sunspot umbra.

a similar size to the umbra to be investigated. Both the temporal and spatial filtering bandpasses are multiplied (in Fourier space) by a Gaussian envelope to reduce edge effects once transformed back into the space/time domain, hence the frequency ranges stipulated above are representative of the full width at half maximum of the corresponding k–ω filter. It is clear from Figure 2 that, within the chosen k–ω filter, there is a very strong oscillatory power signal, which is approximately seven orders of magnitude above the background. The overall k–ω diagram depicts many of the quiet-Sun and internetwork features documented by Krijger et al. (2001), Kneer & Bello González (2011), and Jess et al. (2012b), whereby higher temporal frequencies tend to be synonymous with larger spatial wavenumbers, producing the diagonal arm of enhanced oscillatory power seen in Figure 2. However, within the boundaries of the applied k–ω filter, there is considerably elevated oscillatory power that spans a multitude of spatial scales (particularly within the range of $0.45 < k < 0.90$ arcsec^{-1}), yet remains relatively discrete in terms of the temporal frequency. This implies that the wave motion is best categorized by a narrow frequency range, yet demonstrates coherency across a broad spectrum of spatial scales, ranging from those close to the diameter of the sunspot umbra ($\approx 13''5$), through to those of similar size to the umbral radius, as indicated by the vertical dashed and dotted lines in Figure 2, respectively.

Oscillatory power, albeit reduced, is still clearly evident at smaller spatial wavenumbers than those associated with the umbral diameter. This implies that the discrete frequencies found within the umbra are still prevalent on much larger spatial scales, including outside the umbral waveguide. From the pioneering work of Ulrich (1970) and Deubner (1975), which has subsequently been thoroughly developed by the use of modern, more sensitive instrumentation and techniques (e.g., Kosovichev et al. 1997; Rhodes et al. 1997; Haber et al. 1999; Christensen-Dalsgaard 2002; Howe et al. 2004; González Hernández et al. 2006, to name but a few), significant p-mode power at similar temporal frequencies (i.e., ≈ 3 minutes) has been found to coherently extend out to spatial wavelengths on the order of 100 Mm ($\sim 140''$), corresponding to wavenumbers $k \sim 0.05$ arcsec^{-1}. This is bigger than our current field of view and indicates that large-scale coherent wave power readily exists in the solar photosphere at the temporal frequencies examined here. Of course, the Hα observations presented in the current study are not only chromospheric in their composition (forming ~ 1500 km above the photosphere), but the presence of a highly magnetic sunspot embedded within the atmosphere naturally adds complexity to the picture (see, e.g., the recent review by Cally et al. 2016). Through multi-wavelength investigations, Rajaguru et al. (2010, 2013) have demonstrated how sunspot structures can modify the observable characteristics of underlying 3-minute p-mode oscillations. Hence, a combination of chromospheric resonances and modified upwardly propagating p-mode oscillations may be the cause of the elevated wave power found at spatial scales exceeding that of the umbral diameter. Indeed, it seems likely that the observed heightened oscillatory power within the sunspot umbra may also be linked to the ubiquitous underlying
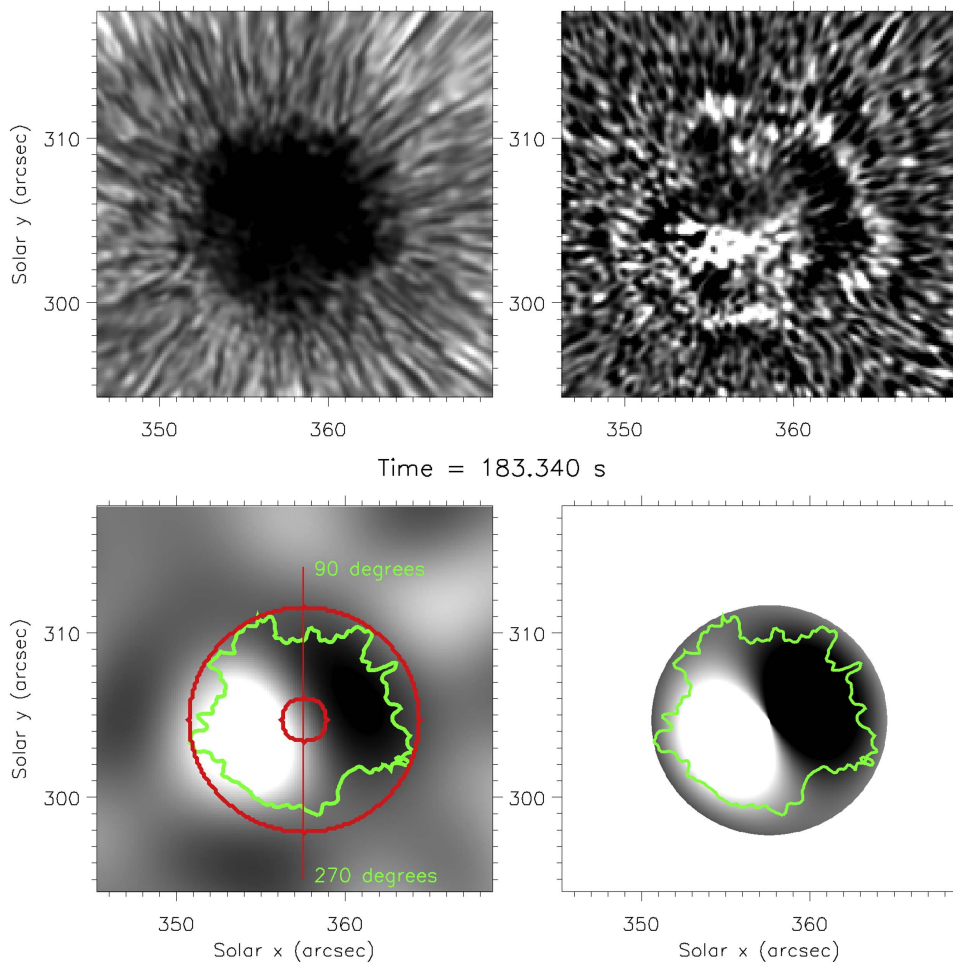
Figure 3. Zoom-in of the unfiltered Hα sunspot umbra (upper left). The upper right panel displays a simultaneous snapshot of the Hα sunspot umbra having first been temporally filtered with a 160–200 s bandpass filter, while the lower left panel reveals the simultaneous intensity fluctuations following the application of an additional 0.45–0.90 arcsec^{-1} wavenumber filter, which reveals clear out-of-phase amplitude fluctuations at opposite edges of the sunspot umbra. The lower right panel is the modeled density perturbation caused by an $m = 1$ slow kink mode oscillation, which has been scaled to match the spatial size of the observed umbra for clarity.

(An animation of this figure is available.)

p-mode oscillations. As per the work of Rajaguru et al. (2010, 2013), a multi-wavelength study (including photospheric observations) is necessary to examine the two-dimensional phase relationships with atmospheric height in order to conclusively verify whether the global p-modes are responsible for the observed wave power at large spatial scales. At spatial scales smaller than the umbral radius (i.e., $k > 0.90$ arcsec^{-1}), the oscillatory power begins to decrease rapidly, while also shifting to slightly higher temporal frequencies in agreement with previously observed ($m = 0$) magneto-acoustic wave phenomena (e.g., Krijger et al. 2001; Kneer & Bello González 2011; Jess et al. 2012b). However, importantly, the lack of a positively correlated relationship between increasing k and ω values within the chosen k–ω filter is not consistent with previous observations of traditional p-mode generated $m = 0$ magneto-acoustic waves (e.g., Duvall et al. 1988), hinting at the presence of a more elusive wave mode.

Once the Hα image sequence had been passed through the k–ω filter, it became very obvious from the resulting time series that large-scale spatially coherent oscillations were manifesting within the chromospheric sunspot umbra, as indicated in the k–ω diagram displayed in Figure 2 and revealed in Figure 3 (and the corresponding movie). The movie linked to Figure 3

documents a 10-minute comparison between the unfiltered (raw), temporally filtered, and spatially *and* temporally filtered time series, in addition to the numerically modeled oscillations (see below), with simultaneous snapshots visible in the panels of Figure 3. Due to the azimuthal rotation about the umbral barycenter (central pivot of the annulus displayed in the lower left panel of Figure 3, and visible in the associated movie), the intensities are averaged in the radial direction across the width of the annulus (40 pixels, or 5″.5). This is in agreement with the k–ω diagram presented in Figure 2, whereby the frequency of oscillation contained within the chosen k–ω filter remains independent of the spatial scale (e.g., the radius from the umbral barycenter), thus implying a rotation with constant angular frequency about the center of the sunspot umbra. Following the radial averaging of the umbral intensities, a polar transformation is performed to convert the azimuthal angle into a linearized array. Stacking these on top of one another produces the time–azimuth diagram shown in the lower right panel of Figure 1. Here, in a similar way to traditional time–distance diagrams, the gradients present in the time–azimuth panel relate to the rotational velocities, or more precisely, the angular frequencies (i.e., rad s^{-1} or deg s^{-1}) of the wave mode. These are measured by following the

techniques defined by Morton et al. (2012) and Jess et al. (2016), whereby a Gaussian profile is first fitted across the widths of the diagonal peaks (bright ridges) and troughs (dark ridges), before fitting a line-of-best-fit to the resulting Gaussian peaks and minimizing the sum of the squares of the residuals (i.e., least-squares fitting; see the solid red line in the lower right panel of Figure 1). This provides angular frequencies of 0.037 ± 0.007 rad s^{-1} (2.1 ± 0.4 deg s^{-1}), corresponding to periodicities of ≈ 170 s, which (as expected) is within the range of the applied k–ω filter (160–200 s), yet more precisely quantifies the embedded temporal frequencies.

To model this wave, we consider the sunspot to be a cylindrical structure in the polar coordinate system (r, ϕ, z), with the z-axis aligned with the umbral magnetic field, using the associated wavenumbers m and k_z (following standard notation). We consider a plasma that changes its conditions (density, temperature, magnetic field) from the internal values (denoted with subscript "i") to the external values (denoted with subscript "e") with a step function. We take the center of the sunspot as being a low-β plasma, with a sound speed of $V_{\mathrm{si}} = 6$ km s^{-1} and Alfvén speed of $V_{\mathrm{Ai}} = 12$ km s^{-1}. These choices are consistent with the Maltby "M" model used by Jess et al. (2013) for the same sunspot structure. Exterior to the sunspot, we consider an unmagnetized ($V_{\mathrm{Ae}} = 0$ km s^{-1}) fluid with a sound speed $V_{\mathrm{se}} = 9$ km s^{-1}. From the total pressure balance, we compute that the exterior is 3.4 times more dense than the interior of the sunspot. We now solve numerically the dispersion relation (as derived by Zaitsev & Stepanov 1975; Edwin & Roberts 1983) for slow waves in a cylindrical configuration. Given the observed behavior, we take an azimuthal dependence of $m = 1$. Moreover, we take $k_{zR} = 30$ (inspired by Moreels et al. 2013; Freij et al. 2016), where R is the radius of the waveguide. For these parameters, we obtain a phase speed of $\omega / k_z = 6.0$ km s^{-1}. Next, we computed the eigenfunctions of these waves in our assumed cylindrical configuration. To that end, we have used Equations (14)–(23) of Yuan & Van Doorsselaere (2016), which relate the physical variables (ρ, T, v_z) to Bessel eigenfunctions. The main difference with the calculation in Yuan & Van Doorsselaere (2016) is that all wave perturbations (in particular, the density and temperature) were put proportional to $\cos(\omega t - \phi)$. These perturbations were then added to the background density (assuming that the radial displacement of the oscillation is small, as would be expected for a slow-mode wave) to produce the image shown in the lower right panel of Figure 3. Here, the radius of the cylindrical waveguide has been scaled, for clarity, to match the spatial size of the observed umbra, thus allowing a direct comparison to be made between the observed and simulated wave amplitudes displayed in the lower left and lower right panels, respectively, of Figure 3. In addition, the movie linked to Figure 3 in the online edition displays the time evolution of the modeled $m = 1$ slow magneto-acoustic mode, which is repeated continuously throughout the duration of the movie. Comparing the modeled wave signatures to those observed in our filtered observations reveals a remarkable level of consistency, further strengthening our interpretation that we have identified, for the first time, evidence for an $m = 1$ slow magneto-acoustic wave propagating in the chromospheric umbra of a sunspot.

While deriving the dispersion relation for the standard cylindrical case, we placed all perturbed variables proportional to $e^{i(k_z z + m\phi - \omega t)}$. Considering the real part of the perturbations

yields a displacement proportional to $\cos(k_z z + \phi - \omega t)$, in which $m = 1$ for the kink asymmetry. When plotting these eigenfunctions as a function of time, they would be represented by anti-clockwise cork-screwing regions of high density along ϕ and z that propagate upwards. Traditionally, for example, in the case of coronal loop oscillations, we see propagating kink waves that oscillate in a plane. To model such instances, the solutions $\cos(k_z z + \phi - \omega t)$ and $\cos(k_z z - \phi - \omega t)$ are added together, which represent the $m = 1$ and $m = -1$ modes, respectively. Simplification of the resulting motion would provide the displacement relation $\cos(k_z z - \omega t)\cos(\phi)$, where $\cos(\phi)$ is a steady-state component no longer dependent on t or z. Ultimately, adding the $m = 1$ and $m = -1$ modes together produces a wave that only propagates in the z-direction (i.e., becomes a standing wave in the ϕ direction). In this case, however, we only consider the $m = 1$ eigenfunction (i.e., not $m = -1$) because we wish to maintain the propagation behavior in the ϕ direction (i.e., the apparent azimuthal motion). Because our Hα observations correspond to the upper chromospheric layer, it is not important for our present study whether the resulting wave is standing or propagating in the z-direction. Here, this distinction results from the superposition of independent waves with $\pm k_z$, and is something that will be investigated using simultaneous, multi-wavelength observations in a follow-up publication.

Alternatively, the observed angular frequency may be the consequence of the superposition of two perpendicularly polarized slow, kink waves, which are standing waves in their respective ϕ directions. Here, the initial conditions would require that two independent $m = \pm 1$ slow kink waves are present, which are 90° out of phase in ϕ: (1) $\cos(k_z z - \omega t)\cos(\phi)$ and (2) $-\sin(k_z z - \omega t)\sin(\phi)$. The superposition of these two kink modes produces a density perturbation relation $\cos(k_z z + \phi - \omega t)$, which is identical to the fluctuations produced from a single, isolated $m = 1$ slow kink mode. Therefore, while the driving mechanism for the observed wave behavior may be different (e.g., a single, isolated $m = 1$ slow kink mode or a pair of perpendicularly polarized $m = \pm 1$ slow kink waves), the wave signatures produced (and observed) are identical.

It must be noted that while our observations clearly indicate apparent azimuthal motion related to the embedded density perturbations of the slow kink mode, this is distinctly different to the rotational twisting associated with torsional Alfvén waves. In the case of Alfvén waves, the physical bulk periodic rotation of magnetic field isocontours is a signature of such wave motion. Observationally, this may manifest as either the visible rotation of the magnetic feature (if well-resolved by the telescope), asymmetric Doppler velocities at opposite sides of the magnetic structure (e.g., De Pontieu et al. 2014; Srivastava et al. 2017), or as periodic changes in the non-thermal line widths of the spectral lines used to observe the feature (e.g., Banerjee et al. 1998; Jess et al. 2009). For a more in-depth review, we refer the reader to the work of Zaqarashvili & Erdélyi (2009) and Mathioudakis et al. (2013). However, in the case of the present analysis, no physical rotation of the sunspot (periodic or otherwise) is observed. Instead, we identify the bulk azimuthal rotation of Fourier power peaks inside the umbra, which are introduced by the density perturbations created from the presence of a single, isolated $m = 1$ slow kink mode or a pair of perpendicularly polarized $m = \pm 1$ slow kink waves. These signatures relate to the presence of the embedded wave mode (i.e., relative phase relationships across the spatial
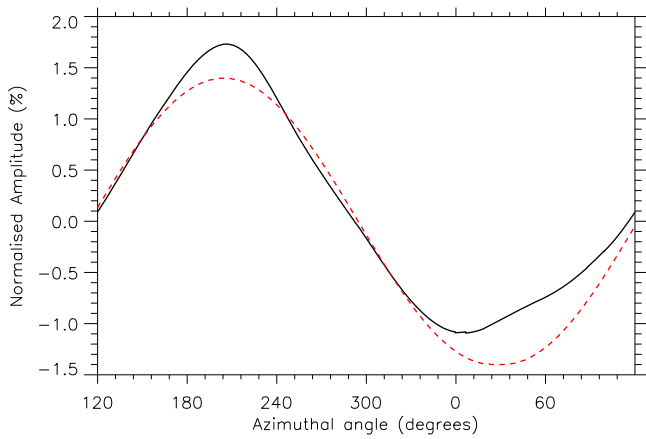
Figure 4. Radially averaged intensity fluctuations contained within the red annulus (lower left panel of Figure 3; see also the dashed green line in the lower right panel of Figure 1) as a function of azimuthal angle around the umbral barycenter. The solid black line represents the amplitudes extracted from the observational Hα data, while the dashed red line corresponds to the predicted amplitudes that are output from our cylindrical model for an $m = 1$ slow magneto-acoustic kink mode.

confines of the umbra), rather than a physical motion of the solar plasma. In addition, the signatures deduced in the present study are also distinctly different from those that would be associated with a fast kink mode. Here, the velocity components (i.e., the plasma flow field of the wave perturbations) are in the vertical direction, while a fast kink mode would be characterized by horizontal velocity perturbations. Furthermore, the intensity (i.e., density) fluctuations associated with fast kink modes would be significantly diminished as a result of the near incompressibility of these waves.

An interesting test to verify the robustness of our interpretation is to plot the instantaneous wave amplitudes as a function of azimuthal angle around the sunspot umbra, as defined by the annulus depicted in Figures 1 and 3. Following the polar transformation, the dashed green line in the lower right panel of Figure 1 represents the instantaneous intensity fluctuations around the circumference of the annulus. These intensities are displayed in Figure 4, whereby a peak-to-peak amplitude is on the order of 2.8% above the background, which is of the same order, albeit slightly smaller, as previous measurements of magnetically confined slow-mode waves in the lower solar atmosphere (e.g., Jess et al. 2007; Beck et al. 2012; Grant et al. 2015). The reduced peak-to-peak amplitude of the $m = 1$ mode is likely a result of the relatively inefficient excitation mechanism for this mode, and hence why the identification of such slow magneto-acoustic modes have proven impossible until the combination of modern high-resolution data sets and Fourier filtering techniques. Furthermore, as would be expected of an $m = 1$ slow-mode wave, the intensity fluctuations, when plotted as a function of azimuthal angle, provide clear evidence of a single, well-resolved oscillation period. Figure 4 displays both the observed (solid black line) and modeled (dashed red line) intensity fluctuations around the azimuth of the umbra. The similarities between the two curves highlight a continued consistency with our interpretation that we have identified an $m = 1$ slow magneto-acoustic mode in the chromospheric umbra of our sunspot. Any slight misalignments between the modeled azimuthal fluctuations and those observed in our data may be the consequence of, for example, the non-perfect

circular cross-section of the sunspot, shifts in the inclination angles of the umbral magnetic fields, which affect the visible compressions of the localized plasma (e.g., Sych & Nakariakov 2014; Krishna Prasad et al. 2015), or from changes in the opacity across the diameter of the sunspot, which may modify the magnitude of the observed intensity fluctuations (e.g., Jensen & Maltby 1965; Khomenko et al. 2003; Felipe et al. 2014).

Of particular interest is the fact that the $m = 1$ slow-mode wave is not omnipresent throughout the duration of the time series. The movie linked to Figure 3 displays the visible manifestation, approximately three complete oscillation cycles, then the disappearance of the $m = 1$ oscillation. This is in stark contrast to the ubiquitous $m = 0$ slow-mode waves that thrive throughout all umbral time series. What is the reason behind this? Are the driving mechanisms completely different, therefore, requiring special circumstances to induce the $m = 1$ mode, which by itself may be a relatively inefficient wave driver? Or, if driven by the underlying p-mode oscillations, could the broadness of this spectrum induce various $m = 1$ modes at fractionally different angular frequencies, thus giving rise to beat phenomena that can modulate the signals produced by the (already weak) driver? Or, finally, could the not quite perfectly cylindrical shape of the sunspot umbra introduce slight differences between any $m = 1$ and $m = -1$ eigenfunctions that might be present? Indeed, Norton et al. (1999) found evidence for 3-minute magneto-acoustic oscillations surrounding the darkest central portion of an irregularly shaped sunspot umbra, though the Fourier power maps presented did not allow any temporal variability to be investigated. Perhaps, in such a regime, additional beating of these two modes (on top of what might be present from $m = 1$ modes at fractionally different angular frequencies) might occur, thus introducing a quasi-periodic nature of the observed wave phenomenon.

4. Conclusions

Here, we have presented high spatial and temporal resolution Hα observations, captured by the HARDcam instrument at the DST, of wave activity in the umbra of a sunspot. On the date of the observations, 2011 December 10, the sunspot corresponding to active region NOAA 11366 was very quiet and exhibited near-circular geometry. Within the immediate vicinity of the sunspot, a k–ω diagram revealed the traditional trend of lower-frequency oscillations being associated with larger spatial scales (e.g., as detailed in Jess et al. 2013). However, of particular interest, was a region of high oscillatory power, which corresponded to a constant frequency (≈ 5.9 mHz, ≈ 170 s or ≈ 0.037 rad s^{-1}) over a wide range of spatial wavenumbers ($0.45 < k < 0.90$ arcsec^{-1} or $7''$–$14''$). Through the application of a k–ω filter, this oscillation was isolated and further studied.

Through modeling the sunspot as a cylindrical structure in the polar coordinate system (r, ϕ, z), with the z-axis aligned with the umbral magnetic field, we solved the intrinsic dispersion relation for an $m = 1$ slow-mode wave and computed the corresponding eigenfunctions. We find that the modeled density perturbations remain consistent with our high-resolution observations, suggesting that we have uncovered a large-scale isolated $m = 1$ slow kink mode oscillation in the chromospheric umbra of a sunspot. However, through analysis of the mathematical eigenfunctions, our observations may also

be consistent with a pair of perpendicularly polarized $m = \pm 1$ kink waves. While the wave signatures produced will be identical, the underlying driving mechanism may be vastly different; something that will require further study, utilizing a plethora of multi-wavelength observations. Thus, for the first time, we have presented a detailed examination of slow kink mode oscillations in the chromospheric umbra of a sunspot, which display spatial coherency on distances of up to $14''$ (or $k \approx 0.45$).

References

Arber, T. D., Brady, C. S., & Shelyag, S. 2016, ApJ, 817, 94
Banerjee, D., Teriaca, L., Doyle, J. G., & Wilhelm, K. 1998, A&A, 339, 208
Beck, C., Rezaei, R., & Puschmann, K. G. 2012, A&A, 544, A46
Beckers, J. M., & Tallant, P. E. 1969, SoPh, 7, 351
Bel, N., & Leroy, B. 1977, A&A, 55, 239
Bloomfield, D. S., Lagg, A., & Solanki, S. K. 2007, ApJ, 671, 1005
Botha, G. J. J., Arber, T. D., Nakariakov, V. M., & Zhugzhda, Y. D. 2011, ApJ, 728, 84
Braun, D. C., Duvall, T. L. J., & Labonte, B. J. 1987, ApJL, 319, L27
Cally, P. S. 1995, ApJ, 451, 372
Cally, P. S. 2017, MNRAS, 466, 413
Cally, P. S., Crouch, A. D., & Braun, D. C. 2003, MNRAS, 346, 381
Cally, P. S., & Moradi, H. 2013, MNRAS, 435, 2589
Cally, P. S., Moradi, H., & Rajaguru, S. P. 2016, GMS, 216, 489
Christensen-Dalsgaard, J. 2002, RvMP, 74, 1073
Christopoulou, E. B., Skodras, A., Georgakilas, A. A., & Koutchmy, S. 2003, ApJ, 591, 416
Cram, L. E., & Wilson, P. R. 1975, SoPh, 41, 313
Crouch, A. D., & Cally, P. S. 2003, SoPh, 214, 201
De Moortel, I. 2006, RSPTA, 364, 461
De Pontieu, B., Rouppe van der Voort, L., McIntosh, S. W., et al. 2014, Sci, 346, 1255732
Deubner, F.-L. 1975, A&A, 44, 371
Duvall, T. L., Jr., Harvey, J. W., Libbrecht, K. G., Popp, B. D., & Pomerantz, M. A. 1988, ApJ, 324, 1158
Edwin, P. M., & Roberts, B. 1983, SoPh, 88, 179
Fedun, V., Shelyag, S., & Erdélyi, R. 2011a, ApJ, 727, 17
Fedun, V., Verth, G., Jess, D. B., & Erdélyi, R. 2011b, ApJL, 740, L46
Felipe, T., Socas-Navarro, H., & Khomenko, E. 2014, ApJ, 795, 9
Fleck, B., & Schmitz, F. 1991, A&A, 250, 235
Freij, N., Dorotovič, I., Morton, R. J., et al. 2016, ApJ, 817, 44
Freij, N., Scullion, E. M., Nelson, C. J., et al. 2014, ApJ, 791, 61

Fujimura, D., & Tsuneta, S. 2009, ApJ, 702, 1443
Gary, G. A. 2001, SoPh, 203, 71
Goldreich, P., & Keeley, D. A. 1977, ApJ, 212, 243
Goldreich, P., & Kumar, P. 1988, ApJ, 326, 462
González Hernández, I., Komm, R., Hill, F., et al. 2006, ApJ, 638, 576
Grant, S. D. T., Jess, D. B., Moreels, M. G., et al. 2015, ApJ, 806, 132
Grant, S. D. T., Jess, D. B., Zaqarashvili, T. V., et al. 2017, NatPh, under review
Haber, D., Jain, R., & Zweibel, E. G. 1999, ApJ, 515, 832
Havnes, O. 1970, SoPh, 13, 323
Henriques, V. M. J., & Kiselman, D. 2013, A&A, 557, A5
Henriques, V. M. J., Scullion, E., Mathioudakis, M., et al. 2015, A&A, 574, A131
Hindman, B. W., Jain, R., & Zweibel, E. G. 1997, ApJ, 476, 392
Howe, R., Komm, R. W., Hill, F., Haber, D. A., & Hindman, B. W. 2004, ApJ, 608, 562
Jain, R., Hindman, B. W., & Zweibel, E. G. 1996, ApJ, 464, 476
Jensen, E., & Maltby, P. 1965, ApNr, 10, 17
Jess, D. B., Andić, A., Mathioudakis, M., Bloomfield, D. S., & Keenan, F. P. 2007, A&A, 473, 943
Jess, D. B., De Moortel, I., Mathioudakis, M., et al. 2012a, ApJ, 757, 160
Jess, D. B., Mathioudakis, M., Christian, D. J., et al. 2010, SoPh, 261, 363
Jess, D. B., Mathioudakis, M., Erdélyi, R., et al. 2009, Sci, 323, 1582
Jess, D. B., Morton, R. J., Verth, G., et al. 2015, SSRv, 190, 103
Jess, D. B., Reznikova, V. E., Ryans, R. S. I., et al. 2016, NatPh, 12, 179
Jess, D. B., Reznikova, V. E., Van Doorsselaere, T., Keys, P. H., & Mackay, D. H. 2013, ApJ, 779, 168
Jess, D. B., Shelyag, S., Mathioudakis, M., et al. 2012b, ApJ, 746, 183
Kato, Y., Steiner, O., Hansteen, V., et al. 2016, ApJ, 827, 7
Kato, Y., Steiner, O., Steffen, M., & Suematsu, Y. 2011, ApJL, 730, L24
Khomenko, E., & Collados, M. 2006, ApJ, 653, 739
Khomenko, E., & Collados, M. 2015, LRSP, 12, 6
Khomenko, E., Collados, M., & Felipe, T. 2008, SoPh, 251, 589
Khomenko, E. V., Collados, M., & Bellot Rubio, L. R. 2003, ApJ, 588, 606
Kneer, F., & Bello González, N. 2011, A&A, 532, A111
Kobanov, N. I., Chelpanov, A. A., & Kolobov, D. Y. 2013, A&A, 554, A146
Kobanov, N. I., Kolobov, D., & Chelpanov, A. 2015, SoPh, 290, 363
Kobanov, N. I., Kolobov, D. Y., Chupin, S. A., & Nakariakov, V. M. 2011, A&A, 525, A41
Kosovichev, A. G., Schou, J., Scherrer, P. H., et al. 1997, SoPh, 170, 43
Krijger, J. M., Rutten, R. J., Lites, B. W., et al. 2001, A&A, 379, 1052
Krishna Prasad, S., Banerjee, D., Van Doorsselaere, T., & Singh, J. 2012, A&A, 546, A50
Krishna Prasad, S., Jess, D. B., & Khomenko, E. 2015, ApJL, 812, L15
Leenaarts, J., Carlsson, M., & Rouppe van der Voort, L. 2012, ApJ, 749, 136
Leenaarts, J., Pereira, T. M. D., Carlsson, M., Uitenbroek, H., & De Pontieu, B. 2013, ApJ, 772, 90
Locans, V., Skerse, D., Staude, J., & Zhugzhda, I. D. 1988, A&A, 204, 263
Löhner-Böttcher, J., & Bello González, N. 2015, A&A, 580, A53
Löhner-Böttcher, J., Bello González, N., & Schmidt, W. 2016, AN, 337, 1040
Maltby, P., Avrett, E. H., Carlsson, M., et al. 1986, ApJ, 306, 284
Mathioudakis, M., Jess, D. B., & Erdélyi, R. 2013, SSRv, 175, 1
McEwan, M. P., & De Moortel, I. 2006, A&A, 448, 763
Moreels, M. G., Freij, N., Erdélyi, R., Van Doorsselaere, T., & Verth, G. 2015a, A&A, 579, A73
Moreels, M. G., Goossens, M., & Van Doorsselaere, T. 2013, A&A, 555, A75
Moreels, M. G., Van Doorsselaere, T., Grant, S. D. T., Jess, D. B., & Goossens, M. 2015b, A&A, 578, A60
Morton, R. J., Verth, G., Jess, D. B., et al. 2012, NatCo, 3, 1315
Mumford, S. J., & Erdélyi, R. 2015, MNRAS, 449, 1679
Mumford, S. J., Fedun, V., & Erdélyi, R. 2015, ApJ, 799, 6
Nagashima, K., Sekii, T., Kosovichev, A. G., et al. 2007, PASJ, 59, S631
Norton, A. A. 2000, PhD thesis, Univ. California
Norton, A. A., & Ulrich, R. K. 2000, SoPh, 192, 403
Norton, A. A., Ulrich, R. K., Bush, R. I., & Tarbell, T. D. 1999, ApJL, 518, L123
Pesnell, W. D., Thompson, B. J., & Chamberlin, P. C. 2012, SoPh, 275, 3
Rajaguru, S. P., Couvidat, S., Sun, X., Hayashi, K., & Schunker, H. 2013, SoPh, 287, 107
Rajaguru, S. P., Wachter, R., Sankarasubramanian, K., & Couvidat, S. 2010, ApJL, 721, L86
Reznikova, V. E., Shibasaki, K., Sych, R. A., & Nakariakov, V. M. 2012, ApJ, 746, 119
Rhodes, E. J., Jr., Kosovichev, A. G., Schou, J., Scherrer, P. H., & Reiter, J. 1997, SoPh, 175, 287
Rijs, C., Rajaguru, S. P., Przybylski, D., et al. 2016, ApJ, 817, 45

Rimmele, T. R. 2004, Proc. SPIE, 5490, 34
Santamaria, I. C., Khomenko, E., & Collados, M. 2015, A&A, 577, A70
Santamaria, I. C., Khomenko, E., Collados, M., & de Vicente, A. 2016, A&A, 590, L3
Schmieder, B. 1977, SoPh, 54, 269
Schou, J., Scherrer, P. H., Bush, R. I., et al. 2012, SoPh, 275, 229
Shelyag, S., Khomenko, E., de Vicente, A., & Przybylski, D. 2016, ApJL, 819, L11
Shelyag, S., & Przybylski, D. 2014, PASJ, 66, S9
Snow, B., Botha, G. J. J., & Régnier, S. 2015, A&A, 580, A107
Socas-Navarro, H., McIntosh, S. W., Centeno, R., de Wijn, A. G., & Lites, B. W. 2009, ApJ, 696, 1683
Srivastava, A. K., Shetye, J., Murawski, K., et al. 2017, NatSR, 7, 43147
Staude, J., Zhugzhda, I. D., & Locans, V. 1985, SoPh, 95, 37
Sych, R. 2016, GMS, 216, 467
Sych, R., & Nakariakov, V. M. 2014, A&A, 569, A72
Ulmschneider, P., Nowak, T., Bohn, U., & Kalkofen, W. 1977, A&A, 54, 61

Ulrich, R. K. 1970, ApJ, 162, 993
Vecchio, A., Cauzzi, G., Reardon, K. P., Janssen, K., & Rimmele, T. 2007, A&A, 461, L1
Verth, G., & Jess, D. B. 2016, GMS, 216, 431
Vigeesh, G., Fedun, V., Hasan, S. S., & Erdélyi, R. 2012, ApJ, 755, 18
Wittmann, A. 1969, SoPh, 7, 366
Wöger, F., von der Lühe, O., & Reardon, K. 2008, A&A, 488, 375
Yuan, D., Nakariakov, V. M., Huang, Z., et al. 2014a, ApJ, 792, 41
Yuan, D., Sych, R., Reznikova, V. E., & Nakariakov, V. M. 2014b, A&A, 561, A19
Yuan, D., & Van Doorsselaere, T. 2016, ApJS, 223, 23
Zaitsev, V. V., & Stepanov, A. V. 1975, Issledovaniia Geomagnetizmu Aeronomii i Fizike Solntsa, 37, 11
Zaqarashvili, T. V., & Erdélyi, R. 2009, SSRv, 149, 355
Zharkov, S., Shelyag, S., Fedun, V., Erdélyi, R., & Thompson, M. J. 2013, AnGeo, 31, 1357
Zhugzhda, Y. D. 2008, SoPh, 251, 501
Zhugzhda, Y. D., & Locans, V. 1981, SvAL, 7, 25